

Itinerant density wave instabilities at classical and quantum critical points

Yejun Feng^{1,2*}, Jasper van Wezel³, Jiyang Wang², Felix Flicker⁴, D. M. Silevitch², P. B. Littlewood^{2,5} and T. F. Rosenbaum^{2,6*}

Charge ordering in metals is a fundamental instability of the electron sea, occurring in a host of materials and often linked to other collective ground states such as superconductivity. What is difficult to parse, however, is whether the charge order originates among the itinerant electrons or whether it arises from the ionic lattice. Here we employ high-resolution X-ray diffraction, combined with high-pressure and low-temperature techniques and theoretical modelling, to trace the evolution of the ordering wavevector Q in charge and spin density wave systems at the approach to both thermal and quantum phase transitions. The non-monotonic behaviour of Q with pressure and the limiting sinusoidal form of the density wave point to the dominant role of the itinerant instability in the vicinity of the critical points, with little influence from the lattice. Fluctuations rather than disorder seem to disrupt coherence.

Understanding the formation and evolution of instabilities in electronic systems, from charge and spin order^{1–6} to heavy fermion and high- T_c superconductivity^{7,8}, to insulator–metal transitions⁹, has assumed a central stance in physics for decades. These different ordering mechanisms can compete and coexist—for instance, charge and spin order vying with superconductivity—in both normal¹⁰ and high- T_c materials^{1,3,4}, enriching the phase space of possible physical states. At the same time, isolating the fundamental mechanisms underlying a particular Fermi surface instability becomes key to progress in the field. At stake is not simply fermiology, but the role of quantum critical points and the emergence of non-Fermi-liquid behaviour^{11,12}. Perhaps the quintessential example, going back to the work of Peierls¹³ in the 1950s, is the ongoing debate about the origin of charge-density-wave ordering in numerous compounds. Suggested mechanisms range from Fermi surface nesting and related instabilities in the electronic structure^{14–16} to mediation by electron–phonon coupling effects^{17,18}, to more exotic phenomena such as excitons paired through the screened Coulomb interaction^{19,20}.

In the case of charge (CDW) and spin (SDW) density waves, a continuous gap opening at the Fermi surface at zero temperature is complicated by the presence and potential influence of quantum critical fluctuations. Over the past two decades, there have been several theoretical approaches on quantum phase transitions with a $2k_F$ type of instability^{16,21–23}. This work has mainly focused on cuprates in two dimensions, and differs primarily on subtle issues such as distinguishing between nesting or hot spots, treating curved Fermi surfaces with parallel or non-parallel electron velocities, and modelling commensurate (1/2, 1/2) versus incommensurate states. Given the presence of both bosonic and fermionic degrees of freedom in the theoretical framework, it is still unclear how the $2k_F$ -type quantum phase transition becomes first¹⁶ or second²³ order.

Experimental insight into the evolution of the electronic gap at the Fermi surface is typically provided by angle-resolved

photoemission spectroscopy (ARPES; ref. 24), measurement of the Hall coefficient^{11,25}, or the observation of quantum oscillations⁸. It is important to note, however, that the wavevectors of the incommensurate CDW/SDW order also directly reflect the location and evolution of the associated energy gap in reciprocal space. With improved X-ray diffraction techniques applied over an extended pressure range^{6,26}, it is now possible to finely resolve the evolution of incommensurate wavevectors and the role of an itinerant instability at a pressure-driven quantum critical point. This is a topic rarely discussed in the literature, mainly because direct measurement of the evolution of the wavevector Q by either neutron or X-ray diffraction was previously scarce, limited to low pressures, and of low resolution^{27,28}. Here, using diffraction-resolved incommensurate orders of the CDW in NbSe₂ and the SDW in Cr, we examine the fundamental physics of density wave formation approaching a pressure-driven critical point. We find that an itinerant electron instability plays a dominant role when the order parameter forms, taking on a pure sinusoidal shape unaffected by interactions with other degrees of freedom, and dictates the incipient long-range order at both the thermal and quantum critical points.

Incommensurate wavevector in P – T space

We plot in Fig. 1 both the pressure–temperature (P – T) phase diagram and $Q(T, P)$ for our two model systems: the CDW in 2H-NbSe₂ and the SDW in Cr. Although of different dimensions (two and three dimensions, respectively), the phase behaviour of these two density-wave systems is similar (Fig. 1 insets). Pressure monotonically suppresses T_{DW} , and both quantum phase transitions under pressure have proved to be continuous, with signatures of critical behaviour in both electrical transport and X-ray diffraction^{2,5,25}.

The evolution of $Q(P)$ over a 1.5% reduction in the lattice constant^{2,5} is non-monotonic in the zero-temperature limit, in

¹The Advanced Photon Source, Argonne National Laboratory, Argonne, Illinois 60439, USA. ²The James Franck Institute and Department of Physics, The University of Chicago, Chicago, Illinois 60637, USA. ³Institute for Theoretical Physics, University of Amsterdam, 1090 GL Amsterdam, The Netherlands.

⁴H. H. Wills Physics Laboratory, University of Bristol, Bristol BS8 1TL, UK. ⁵Physical Sciences and Engineering, Argonne National Laboratory, Argonne, Illinois 60439, USA. ⁶Division of Physics, Mathematics, and Astronomy, California Institute of Technology, Pasadena, California 91125, USA.

*e-mail: yejun@anl.gov; tfr@caltech.edu

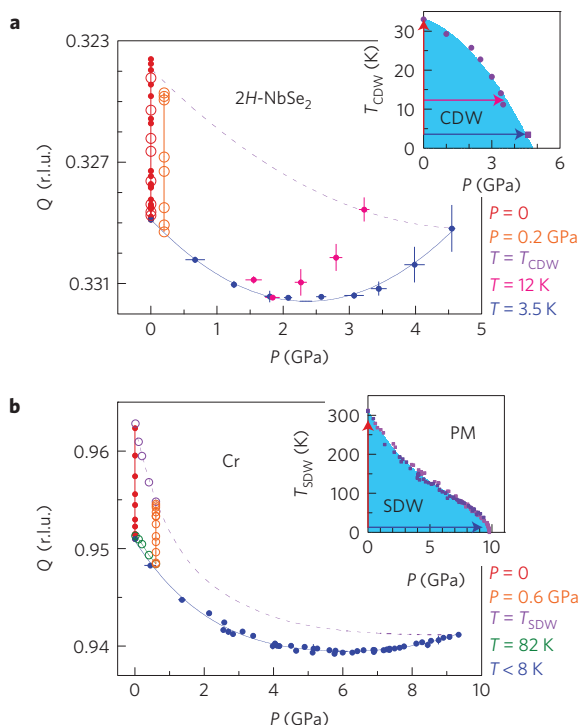


Figure 1 | Pressure-temperature evolution of the incommensurate wavevector Q . **a, b.** Ordering wavevector Q plotted as a function of both temperature T and pressure P . **a.** For CDW in NbSe₂, $Q(T, P)$ with solid symbols are from the current study, whereas open symbols are from refs 28,36, with a shift of all Q by 0.00095 r.l.u. to match our data at $Q(0, 0)$. Vertical error bars represent 1σ s.d. of Q , and horizontal error bars represent the full range of pressure during measurement. **b.** For SDW in Cr, $Q(T, P)$ are collected from the literature (open symbols)²⁷ and our previous work (solid symbols)^{2,49}. Insets: P - T phase diagrams of NbSe₂ (refs 5,31) and Cr (ref. 25) show similar monotonic trends in $T_{DW}(P)$. On the other hand, $Q(P)$ of NbSe₂ and Cr manifest a non-monotonic behaviour in the low-temperature limit. Arrows in phase diagrams mark our measurement trajectories for the data plotted in the main panels.

contrast to the monotonic trend in $T_{DW}(P)$. As we demonstrate below, the ordering wavevector Q at the critical point represents an instability in the electronic structure, corresponds to a maximum in the full electronic susceptibility²¹, and may be related to special features of the electronic bands or its Fermi surface^{14–16}. In real systems with a spatial dimension higher than one, an itinerant instability is typically induced by a bosonic coupling between electronic states at the Fermi surface²¹, with the type of the exchanged boson ranging from photons (Coulomb)^{14,19} and phonons^{17,18}, to magnons (spin fluctuations)^{6,29}. The required finite strength of bosonic coupling has a limiting behaviour towards zero only for perfect nesting, which is exemplified by the original Peierls scenario of $2k_F$ instability of free electron gas in one dimension¹³. With the long-range DW order arising, the value of Q may be tuned by physical processes beyond the band structure, resulting in non-monotonic behaviour in the P - T phase space.

Mean-field evolution of $Q(T, P=0)$

Before discussing the $Q(P)$ behaviour in detail, we survey $Q(T)$ of several CDW/SDW materials at ambient pressure. The materials listed in Fig. 2a have incommensurate ordering existing to the lowest temperature and represent a diverse spectrum of spin or charge origins in various dimensions from one (NbSe₃) to three (Cr, GdSi). Some, such as TbTe₃ (ref. 30), Cr, and GdSi (refs 6,29), have well-established nesting conditions at the Fermi surface, whereas others

such as NbSe₂ are at best described as hot spots²⁴. Nevertheless, all five SDW/CDW states are clearly tied to instabilities of the itinerant electrons, resulting in the formation of gaps in the Fermi surface, with both resistivity anomalies^{25,29–32} and strong changes in the Hall coefficient^{29,33} at the transition. By contrast to $Q(P)$, all of the $Q(T)$ of the CDW/SDW systems in Fig. 2a evolve monotonically with temperature.

McMillan prescribed key elements of a mean-field free-energy expression for an incommensurate CDW/SDW (ref. 34). Here we take the essence of the McMillan theory and neglect both interlayer and multi- Q interactions between CDWs. They are not a common feature of the examples listed above and thus are not expected to be necessary for explaining the $Q(T)$ behaviour. The free-energy density is then^{2,34}:

$$F = a\psi^2 + b\psi^4 + c\xi^2|\nabla\psi|^2 + e\psi^2|\nabla\phi - q|^2 - f\psi^n \cos(n\phi - Gx) \quad (1)$$

The CDW order parameter $\text{Re}(\psi e^{-i\theta})$ has amplitude ψ and phase ϕ . q is the natural wavevector of the CDW determined by a maximum in its full electronic susceptibility, ξ is the spatial correlation length of the CDW, G is a reciprocal lattice unit vector and a, b, c, d, e, f are the coefficients of the individual terms, which be discussed next. The first two terms are leading orders in a Landau free-energy expansion. The third and fourth terms come from the energy costs of distorting a CDW from its ideal condition by stretching/compressing the wave from the wavevector set by the susceptibility, and from having a finite spatial correlation length ξ . For CDWs, these two terms includes both electronic energy from repopulating the Brillouin zone³⁴ and static phonon energy from coupling to the lattice. The fifth term reflects the lock-in effect, which favours a CDW commensurate with the lattice. $Q(T)$ is determined by the competition between the fourth and fifth terms, as ψ grows with decreasing temperature.

This competition is best visualized by plotting $Q(\psi)$ (Fig. 2b), using as examples TTF-TCNQ and 2H-TaSe₂ (refs 35,36). Both CDW systems order incommensurately at high temperature, before experiencing a first-order phase transition to a commensurate state with discontinuities in both Q and ψ . As shown in Fig. 2b, Q is independent of ψ in the $\psi = 0$ limit. As ψ increases, Q evolves continuously until the lock-in transition creates discontinuities in both Q and ψ . At even lower temperature, ψ continues to grow whereas Q remains constant at the commensurate position. For TTF-TCNQ and TaSe₂, $dQ/d\psi$ approaches zero at both small and large ψ , which clearly indicates the alternating dominance of either the fourth or fifth term in equation (1) with different powers of ψ . As exemplified by TTF-TCNQ, the lock-in position can be located far from the intrinsic CDW wavevector $q = Q(T_{DW})$, and ΔQ can be as large as one quarter of the reciprocal lattice unit³⁵. In addition, a lock-in transition does not necessarily exist for every n value; for TTF-TCNQ, the $Q(T)$ evolution passes through $n = 3$ and locks in for $n = 4$. This possibly explains the wavevectors in NbSe₃, GdSi and Cr seemingly moving away from commensurate positions of $n = 4, 2$ and 1 , respectively. For NbSe₂, $n = 3$ was assumed to be the commensurate position, in association with the lock-in transition in TaSe₂ (ref. 34).

For CDWs that remain incommensurate, the $Q(\psi)$ plot in Fig. 2c manifests only partial features of the full evolution demonstrated in Fig. 2b. This indicates that the magnitude of ψ is insufficient for higher-order terms to contribute substantially to the free energy. $Q(\psi)$ behaviour similar to Fig. 2c is also observed for the SDW in Cr at ambient P (Fig. 3a of ref. 2). Hence $Q(\psi)$ provides a direct measure of the relative importance of terms with different powers of ψ for a collection of vastly different density-wave systems. We note that the SDW in Cr possesses no local spin moments,

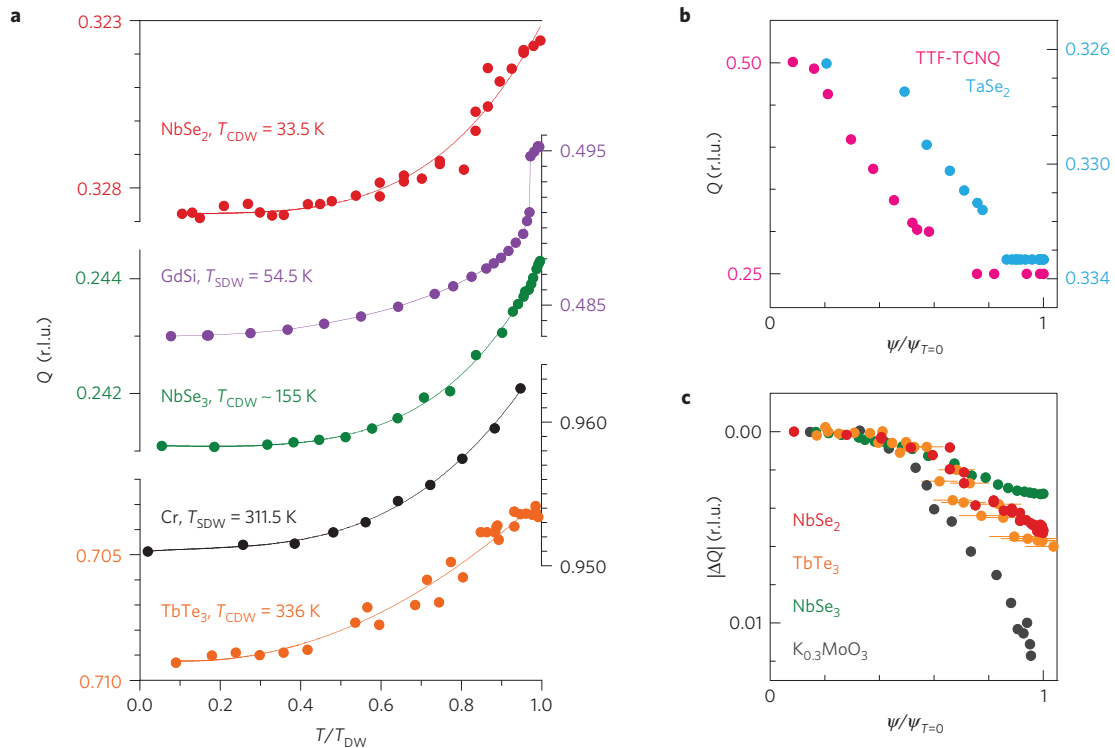


Figure 2 | Temperature evolution of wavevector Q . **a**, Incommensurate $Q(T)$ for CDWs and SDWs arranged by increasing T_{DW} over one decade. **b**, $Q(\psi)$, with temperature as the hidden variable in the range $0 < T < T_{DW}$, are plotted for the CDW systems TTF-TCNQ and TaSe₂, both of which manifest a lock-in transition to a commensurate state. Here, ψ at zero temperature is strong enough such that $Q(\psi)$ shows the full evolution between the two limits of $\psi/\psi_{T=0} = 0$ and 1; each end is dominated by individual terms of different powers of ψ in the free energy of equation (1). **c**, $Q(\psi)$ for CDWs which remain incommensurate at low temperature evolves over only part of the master curve in **b**. $Q(T)$ of NbSe₂ from the current study is compared to data from the literature: NbSe₂ (ref. 36), GdSi (refs 6,29), NbSe₃ (refs 50,51), Cr (ref. 49), TbTe₃ (ref. 30), TaSe₂ (ref. 36), TTF-TCNQ (ref. 35) and K_{0.3}MoO₃ (ref. 52). The CDW amplitude $\psi(T)$ is obtained from X-ray or neutron diffraction intensity $I(T)$ by $I \sim \psi^2$ (ref. 37), and is normalized by its low-temperature limit $\psi_{T=0}$ for comparisons in **b** and **c**. For K_{0.3}MoO₃, the experimental resolution was insufficient to determine whether or not a lock-in transition occurs; no first-order discontinuity was observed in the temperature dependence of either the order parameter or the wavevector⁵².

and that SDW states in Cr and GdSi are not coupled to a lattice distortion at the primary wavevector Q (refs 29,37). Thus, the similar limiting behaviour of $Q(\psi)$ at $\psi = 0$, regardless of SDW or CDW type and coupling mechanism^{6,14,17–19,29}, as shown in Fig. 2 and ref. 2, points to an origin of these instabilities among the itinerant electrons rather than the localized ionic lattice. In general, $Q(\psi)$ provides a macroscopic indicator independent of the microscopic and quantitative details of the DW-lattice coupling. This is reflective of the fact that all $Q(T)$ in Fig. 2 behave similarly despite a variation of over a decade in the ordering temperature T_{DW} .

Harmonics of the incommensurate density wave

For a sinusoidal incommensurate DW with both $\psi(x) = \text{constant}$ and $\phi(x) = Qx$, the last term in equation (1), $f\psi^n \cos(n\phi - Gx)$, will always be zero when summed over all lattice sites, no matter the magnitude of ψ . For a CDW and a collinear SDW, ψ is a scalar and constant in a mean-field framework³⁸, and all deviations of the DW from a pure sinusoid are represented by $\Delta\phi(x) = \phi(x) - Qx$. Experimentally, the deviation of an incommensurate wave from a sinusoidal form is reflected by the presence of higher-order harmonics in the diffraction pattern^{37,39}. For the CDW in NbSe₂, we were able to measure both the primary wave and its second harmonic with our bulk-sensitive, high-resolution X-ray diffraction technique (Fig. 3). Combining measurements at orders such as $(Q, 0, 0)$, $(1 \pm Q, 0, 0)$ and $(2 - Q, 0, 0)$, the amplitude ratio between primary and second harmonics is $\psi_2/\psi_1 = 0.09 \pm 0.02$ at $T = 3.5$ K. No other higher harmonic was observed within our measurement sensitivity (Fig. 3). Similar behaviour in higher harmonics was

observed in the SDW of Cr up to fourth order of the primary wave³⁷. For Cr in the low-temperature limit, the amplitude ratios for SDW/CDW and their higher harmonics are $\psi_3/\psi_1 = 0.018$ and $\psi_4/\psi_2 = 0.019 \pm 0.003$, respectively³⁷, only a factor of five weaker than the ratio ψ_2/ψ_1 in NbSe₂.

The deviation from pure sinusoidal behaviour, $\Delta\phi(x)$, would minimize the free energy in equation (1). One possible solution was proposed by McMillan⁴⁰ as a ‘discommensuration’ state, which has been widely considered as a model for the CDW in NbSe₂. Locally, the CDW state is forced into a perfectly commensurate wavelength of $3a$ by its coupling to the atomic lattice. To satisfy the requirement of having an incommensurate wave on average, the density modulations then develop phase slips of $-2\pi/3$ between neighbouring unit cells at every distance ξ_0 (ref. 40). To create the specific $Q = 1/3 - \delta = 0.3286$ r.l.u. observed at $T = 3.5$ K for NbSe₂, the $-2\pi/3$ phase slips need to be placed at every $1/(3\delta) \sim 70$ unit cells, or a distance $\xi_0 \sim 240$ Å. To have an incommensurate order with a longer wavelength than that of the commensurate order $1/3$ r.l.u., all phase slips also need to have the same value of $-2\pi/3$ and no phase slips of $2\pi/3$ are allowed. A perfectly sharp $-2\pi/3$ phase slip creates many strong higher harmonics that would be readily observable, with amplitude ratios such as $\psi_2/\psi_1 = 0.45$ for first and second harmonics (Fig. 3b). To get agreement with the observed intensity ratios in NbSe₂, we thus find that each phase slip is spread over a distance of the same order of magnitude as ξ_0 . Our measurements show that the modulation of the electron density in the bulk is closer to that of a perfectly incommensurate pattern than the discommensuration form with sharp phase slips

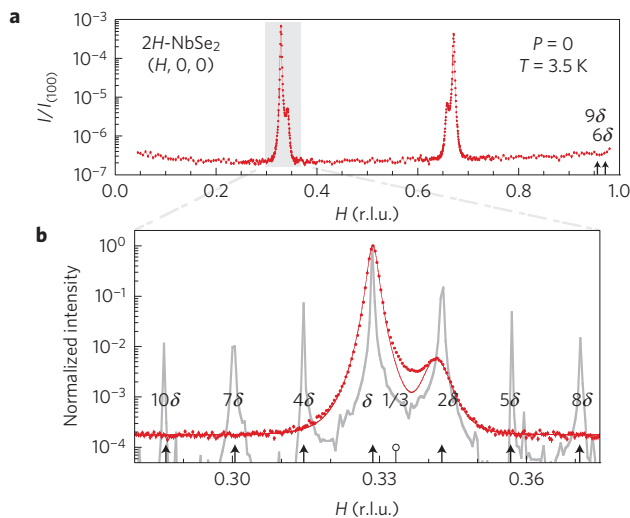


Figure 3 | CDW harmonics in NbSe₂. **a**, Longitudinal ($\theta/2\theta$) scan in reciprocal lattice units (r.l.u.) along the in-plane direction of $(H, 0, 0)$ for NbSe₂. Both the primary and second harmonics of CDW are clearly resolved over the background around mirroring $(Q, 0, 0)$ and $(1 - Q, 0, 0)$ positions. The plotted intensity is normalized to that of the $(1, 0, 0)$ lattice order. Vertical error bars represent 1σ s.d. of counting statistics. **b**, A profile comparison between the experimental observed CDW for NbSe₂ at $(Q, 0, 0)$ (red points) and a simulated diffraction pattern of a discommensurate CDW with phase slips in the sharp limit (grey line)⁴⁰. For comparison, both intensities are normalized to unity at the primary wavevector position. The fine longitudinal CDW scan in **b** was measured with our best instrument resolution (better by a factor of two than the long scan in Fig. 2a; Methods). The data is fitted by the summation of two Lorentzian-squared functions for primary and second harmonics in addition to a constant background (red solid line). Positions of CDW harmonics are marked by black arrows on the horizontal axes in both **a** and **b**, with the separation between the primary incommensurate CDW and the commensurate $(1/3, 0, 0)$ position (white circle) denoted as $\delta = 1/3 - Q$. The separation becomes $m\delta$ for the m th-order harmonic; these are naturally translated by the unit vector of the lattice periodicity, and hence for small δ are observed close to the commensurate position. Harmonics from fourth to tenth orders are not observed even with a CDW signal-to-background ratio larger than 5,000. The simulated diffraction profile for a discommensurate CDW with single-helicity $-2\pi/3$ phase slips over a single unit cell at a regular spacing of 70 unit-cell distance has strong harmonic peaks at all orders within our measurement range⁴¹.

proposed by McMillan and observed in the surface state of NbSe₂ (ref. 41).

Approaching the thermal transition temperature, T_{DW} , the diminishing coupling between the CDW and the lattice is reflected directly in the harmonic behaviour. In Fig. 4, we plot representative diffraction profiles and the temperature evolution of the CDW at $(1 + Q, 0, 0)$. The intensities of both the primary and secondary harmonics of the CDW in NbSe₂ decrease with increasing T . However, the intensity of the second harmonic drops much faster than that of the primary CDW, with a relative ratio between the two evolving in a nearly linear fashion in temperature (Fig. 4 inset). Similar behaviour was seen as well in Cr, where the higher harmonic intensities scale as $I_Q(T) \sim I_{2Q}^{1/2} \sim I_{4Q}^{1/4}$ (ref. 37). We conclude that the density waves due to the itinerant instabilities in NbSe₂ and Cr both have the limiting form of a purely sinusoidal wave at T_{DW} , with a $\Delta\phi(x) \rightarrow 0$.

Evolution of a non-monotonic $Q(T=0, P)$

The non-monotonic behaviour of $Q(T=0, P)$ in Fig. 1 evolves over a range of 0.003–0.012 r.l.u., which is well below the

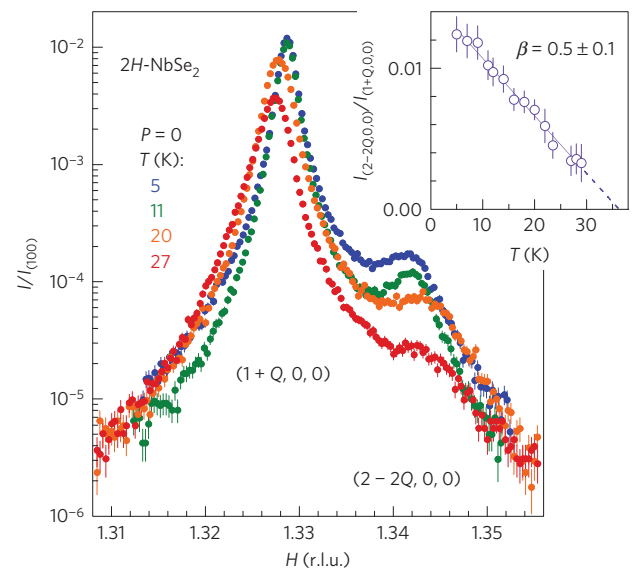


Figure 4 | Temperature evolution of CDW harmonics in NbSe₂.

Representative longitudinal scans of $(1 + Q, 0, 0)$ and $(2 - 2Q, 0, 0)$ at four different temperatures below T_{CDW} . Error bars represent 1σ s.d. of counting statistics. Inset: temperature dependence of the intensity ratio between the second harmonic and the primary CDW, plotted for one single sample. Error bars represent 1σ uncertainty. The intensity ratio was fitted (solid line) to a power law of $I_{(2-2Q,0,0)}/I_{(1+Q,0,0)} \sim (T_{CDW} - T)^{2\beta}$ with $\beta = 0.5 \pm 0.1$ and $T_{CDW} = 36.8 \pm 3.3$ K.

resolution of photoemission techniques²⁴. As density functional theory approaches are still insufficient to describe the SDW ground state in Cr (ref. 42), this subtle non-monotonic behaviour is difficult to resolve with *ab initio* calculations. Here, instead, we argue that $Q(P)$ can be explained by macroscopic free-energy considerations similar to those made for $Q(T)$ at ambient P , once the pressure dependence of the different contributions to the electronic susceptibility are taken into account.

As discussed above, the temperature evolution of the incommensurate wavevector Q starts at the itinerant condition q at T_{DW} and changes to $Q(T=0, P)$ owing to the higher-order lock-in term that pulls Q away from q . The pressure dependence of q also has been measured, as a part of the full $Q(T)$ evolution, at several low pressures up to 0.2 and 0.6 GPa for NbSe₂ and Cr, respectively^{27,28}. Those studies provide valuable information of initial changes in $q(P) = Q(T_{DW}, P)$. From Fig. 1, $q(P)$ is clearly nonlinear, but nevertheless is still probably monotonic, given the small variation of 1.5% in the lattice constant. When the transition temperature T_{DW} decreases towards the quantum critical point, the strength of the order parameter ψ monotonically decreases with P at zero temperature. The competition between the lower-order electronic instability term and the higher-order lock-in term in equation (1) becomes increasingly one-sided with reducing ψ under pressure. This is consistent with the experimental observation that $\Delta Q(P) = q(P) - Q(T=0, P)$ decreases in magnitude under pressure in both NbSe₂ and Cr (refs 27,28; Fig. 1). Eventually, close to the quantum critical point, the lower-order term $\psi^2|\nabla\phi - q|^2$ in equation (1) dominates, and $q(P)$ and $Q(T=0, P)$ converge at P_c . The non-monotonic behaviour in $Q(T=0, P)$ is therefore due to a changing balance between terms of various powers in ψ , in addition to a varying q under pressure. The measured CDW/SDW wavevector at the quantum critical point is a true reflection of a maximum in the full electronic susceptibility arising from features such as (but not limited to) the presence of nesting or hot spots in the electronic structure.

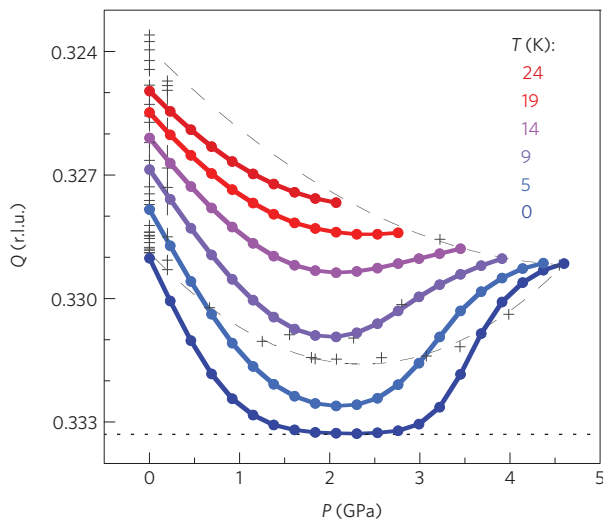


Figure 5 | Theoretical modelling of $Q(T, P)$. The evolution of $Q(T, P)$ is modelled by minimizing the free energy in equation (1) for the CDW in NbSe₂ with optimally spaced and widened phase slips, with the global behaviour controlled by two free parameters. Calculated $Q(P)$ at several fixed temperatures (linked dots) are plotted in comparison with experimental data (grey crosses bound by grey dashed lines, from Fig. 1), capturing the non-monotonic behaviour of $Q(P)$. The simulated results also show a lock-in transition at $T = 0$ (horizontal dashed line).

We model in Fig. 5 the $Q(T, P)$ behaviour for NbSe₂ using the free-energy expression in equation (1), with parameters and coefficients constrained by physical considerations in the following way. For $a(T, P)$, which determines T_{CDW} , its temperature dependence is assumed to be linear, whereas its pressure dependence is determined from the measured phase diagram: $a(T, P) = -a_0(1 - T/T_{\text{CDW}}(P))$. The coefficient $b(T, P)$ for the quartic term is assumed constant, which determines the primary CDW amplitude at $T = 0$ through the ratio b/a . Although the spatial correlation length ξ is pressure dependent⁵, the third term in equation (1), describing spatial variations of the DW amplitude, is neglected in our modelling as it does not directly affect Q . The pressure dependence of the fourth term is directly taken from experimental data as $q(P) = Q(T_{\text{DW}}, P)$, with coefficient e assumed constant. The pressure dependence of the coefficient f of the lock-in term, which arises from the variation of orbital overlaps with pressure, is assumed linear given the small change in the compressed lattice constant. We use McMillan's discommensuration construction to build the phase distortion $\Delta\phi(x)$ (Supplementary Information). The width and density of phase slips in $\phi(x)$ can be varied to minimize the free energy F of equation (1) and the density of phase slips generates the Q value at every point in P - T phase space.

Apart from an overall scaling factor for the magnitude of the free energy, there are only two free parameters left. They describe the ratio of the lock-in energy to the energy cost of deviating from q set by the fourth term in equation (1), as well as the slope of the linear pressure dependence in the lock-in term. Although $\Delta\phi(x)$ minimizes the free energy and determines Q at every P - T point, optimizing those two parameters results in the global behaviour of $Q(T, P)$ in Fig. 5 (Supplementary Information). The qualitative agreement with experimental results in both the magnitude of Q variations, as well as the non-monotonic pressure dependence, is satisfying given the simplicity of approximations used.

$2k_F$ instability at a quantum critical point

In our current study, the CDW state in NbSe₂ was tracked under pressure (Figs 1 and 6) up to the quantum phase boundary at

$P_c = 4.6$ GPa (ref. 5). In addition to wavevector $Q(T, P)$, X-ray diffraction also provides the static CDW correlation length ξ in real space, with $\xi = 600$ Å for our samples at $T = 3.5$ K and ambient pressure (Fig. 6). Whereas the lattice correlation length remains long range to at least 1,500 Å throughout our probed P - T space, ξ gradually decreases as it approaches both the thermal and quantum critical points⁵, similar to thermal behaviour in other SDW/CDWs (refs 37,43). Near both thermal and quantum phase boundaries, ξ is about 26–50 Å in NbSe₂ (Fig. 6), roughly 3–5 CDW wavelengths or 8–15 unit-cell sizes.

The mechanism for destroying long-range static CDW coherence, leading to a shortened ξ , has been attributed to an increase in either fluctuation effects⁵ or disorder pinning^{37,38,43}. At $T = 3.5$ K and $P = 0$, our observed CDW line shape is described by a Lorentzian-squared function (Figs 3b and 6c), which is consistent with disorder pinning the CDW to random phases at impurity sites⁵. A strong pinning picture is unlikely to apply near the transition, as it necessarily introduces many higher harmonics of the CDW, in contrast to our observed temperature evolution (Fig. 4). Approaching either the thermal or quantum phase transitions, the line shape is best described by a pure Lorentzian form (Fig. 6a)^{5,43}, which indicates that the CDW phase correlation is exponentially decaying in real space without experiencing abrupt changes. Although this could be consistent with a pinning picture that allows the CDW phase distortion to be distributed over a spatial range across a pinning site³⁸, the extremely short ξ of 8–15 unit cells in our observation is unlikely to host multiple disorder sites within a coherent volume, necessary to collectively anchor the phase-coherent CDW domain. We conclude that the shortened correlation lengths are more likely due to increasing (quantum or thermal) fluctuation effects at the phase boundaries. Furthermore, $\phi(x)$ is not constrained by disorder, but has the freedom to adjust to the itinerant instability, and the observed incommensurate CDW wavevector Q continuously evolves approaching both the thermal and quantum limits (Fig. 1). Similarly, CDWs remain incommensurate with very short correlation lengths in cuprates^{3,4}, despite significant disorder from doping. Our observation of a sinusoidal, incommensurate density wave and a short correlation length signifies, respectively, the importance of itinerant instability and fluctuation effects at both classical and quantum critical points.

Our study examines $2k_F$ density waves in solid-state materials from a top-down perspective. Pressure tuning helps to identify the itinerant instability as the dominant influence at a quantum critical point, even in the presence of spin, charge, orbital and lattice degrees of freedom. The striking similarity between SDW and CDW systems in both $Q(\psi)$ at ambient P (Fig. 2 and ref. 2) and $Q(T, P)$ over P - T space (Fig. 1) clearly manifests the close relationship between these two types of correlated electron states, regardless of the presence of instabilities among the local ions or spins, or the lack thereof. Our work should motivate attempts to reconcile theories that describe charge and spin instabilities from very different points of view. CDWs originating from itinerant electrons previously have been pooled indifferently with incommensurate lattice systems¹⁸. However, the wavevectors of incommensurate lattice distortions tend to be temperature independent⁴⁴. Based on the observed evolution of $Q(T, P)$ and $Q(\psi)$, our comparative study of CDWs and SDWs emphasizes the universal nature and importance of correlated itinerant pairs, rather than lattice instabilities, in the presence of various choices of coupling mechanisms. In CDWs, even if the itinerant instability is mediated by the Coulomb interaction (phonons), there should still exist additional phonon coupling because of the presence of the localized charge lattice¹⁸. For spins, phonons become largely irrelevant in SDWs, both with and without local moments^{29,37}, mirroring the charge scenario. Directly resolving boson coupling between itinerant electron pairs in traditional CDW/SDW systems or high-temperature cuprates

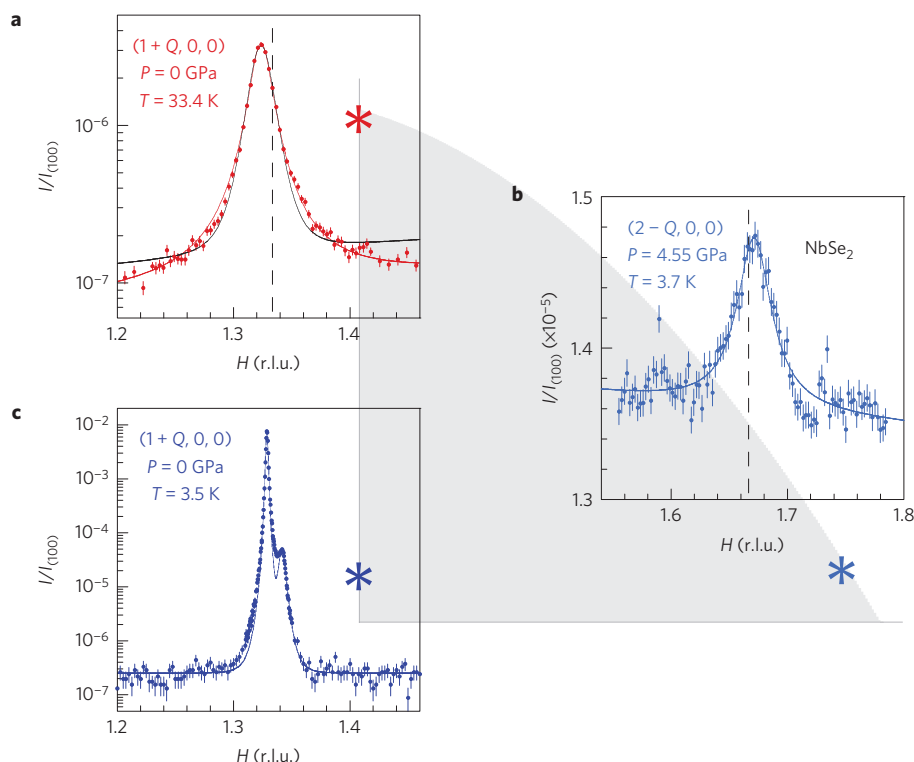


Figure 6 | CDW fluctuations near the thermal and quantum critical points. **a–c**, Longitudinal X-ray diffraction scans for the CDW in NbSe₂. Error bars represent 1σ s.d. of counting statistics. At $(T \sim T_{\text{CDW}}, P=0)$ (**a**) and $(T \rightarrow 0, P \sim P_c)$ (**b**), the CDW line shapes are best fitted with a Lorentzian form plus a linear background (red, **a**; light blue, **b**). At $(T \rightarrow 0, P=0)$ (**c**), the fit to the CDW line shape instead requires the sum of two Lorentzian-squared functions and a constant background (blue, **c**). A Lorentzian-squared form with a linear background (black) is also used to fit data in **a** as a comparison. The vertical dashed lines mark the $1/3$ commensurate position. Locations of all three (T, P) points are marked by asterisks of the same colour on the grey P – T phase diagram in the background. Near the phase boundary, the CDW profile represents a small CDW correlation length ξ , which is ~ 50 Å for $(T \sim T_{\text{CDW}}, P=0)$ and ~ 26 Å for $(T \rightarrow 0, P \sim P_c)$ in the basal plane. The shortened ξ is inconsistent with pinning from disorder and is instead attributed to thermal fluctuations and quantum fluctuations⁵ near their respective critical points.

remains challenging⁴⁵, and time-resolved techniques such as pump–probe ARPES (ref. 46) potentially could provide key insights into the different contributors to the full electronic susceptibility.

In complementary experiments, Fermi surfaces with a nesting instability potentially could be manufactured from a bottom-up approach using cold atoms. Following the early idea of a commensurate nesting condition⁴⁷, recent developments in shaken optical lattices⁴⁸ have pointed to a method to produce customized band structures with incommensurate nesting. As phonons are not naturally present in an optical lattice, the coupling between paired atoms instead comes from the short-range van der Waals interaction, which is nearly q -independent in reciprocal space and could be tuned to be attractive. This is comparable to various interactions between itinerant pairs in solids that are not phonon-mediated, such as the screened Coulomb interaction in excitons^{19,20} or magnons from fluctuations in locally ordered spins²⁹. Alternatively, the electron–phonon interaction may be mirrored in a mixture of fermionic and bosonic atoms in a weak optical potential. A comparison of these different constructions in cold-atom systems could shed further light on itinerant instabilities at quantum critical points^{14,17,18}.

Methods

Methods and any associated references are available in the [online version of the paper](#).

Received 25 May 2015; accepted 26 June 2015;
published online 27 July 2015

References

- Tranquada, J. M., Sternlieb, B. J., Axe, J. D., Nakamura, Y. & Uchida, S. Evidence of stripe correlations of spins and holes in copper oxide superconductors. *Nature* **375**, 561–563 (1995).
- Jaramillo, R. *et al.* Breakdown of the Bardeen–Cooper–Schrieffer ground state at a quantum phase transition. *Nature* **459**, 405–409 (2009).
- Ghiringhelli, G. *et al.* Long-range incommensurate charge fluctuations in (Y,Nd)Ba₂Cu₃O_{6+x}. *Science* **337**, 821–825 (2012).
- Chang, J. *et al.* Direct observation of competition between superconductivity and charge density wave order in YBa₂Cu₃O_{6.67}. *Nature Phys.* **8**, 871–876 (2012).
- Feng, Y. *et al.* Order parameter fluctuations at a buried quantum critical point. *Proc. Natl Acad. Sci. USA* **109**, 7224–7229 (2012).
- Feng, Y. *et al.* Hidden one-dimensional spin modulation in a three-dimensional metal. *Nature Commun.* **5**, 4218 (2014).
- Pfleiderer, C. Superconducting phases of f -electron compounds. *Rev. Mod. Phys.* **81**, 1551–1624 (2009).
- Doiron-Leyraud, N. *et al.* Quantum oscillations and the Fermi surface in an underdoped high- T_c superconductor. *Nature* **447**, 565–568 (2007).
- Imada, M., Fujimori, A. & Tokura, Y. Metal–insulator transitions. *Rev. Mod. Phys.* **70**, 1039–1263 (1998).
- Littlewood, P. B. & Varma, C. M. Gauge-invariant theory of the dynamical interaction of charge density waves and superconductivity. *Phys. Rev. Lett.* **47**, 811–814 (1981).
- Paschen, S. *et al.* Hall-effect evolution across a heavy fermion quantum critical point. *Nature* **432**, 881–885 (2004).
- Löhneysen, H. V., Rosch, A., Vojta, M. & Wölfle, P. Fermi-liquid instabilities at magnetic quantum phase transitions. *Rev. Mod. Phys.* **79**, 1015–1075 (2007).
- Peierls, R. E. *Quantum Theory of Solids* 108–112 (Oxford Univ. Press, 1955).
- Overhauser, A. W. Spin density waves in an electron gas. *Phys. Rev.* **128**, 1437–1452 (1962).
- Rice, T. M. & Scott, G. K. New mechanism for a charge-density-wave instability. *Phys. Rev. Lett.* **35**, 120–123 (1975).

16. Abanov, A. & Chubukov, A. V. Spin-fermion model near the quantum critical point: One-loop renormalization group results. *Phys. Rev. Lett.* **84**, 5608–5611 (2000).
17. Chan, S.-K. & Heine, V. Spin density wave and soft phonon mode from nesting Fermi surfaces. *J. Phys. F* **3**, 795–809 (1973).
18. Johannes, M. D. & Mazin, I. I. Fermi surface nesting and the origin of charge density waves in metals. *Phys. Rev. B* **77**, 165135 (2008).
19. Jérôme, D., Rice, T. M. & Kohn, W. Excitonic insulator. *Phys. Rev. B* **158**, 462–475 (1967).
20. van Wezel, J., Nahai-Williamson, P. & Saxena, S. S. Exciton–phonon-driven charge density wave in TiSe_2 . *Phys. Rev. B* **81**, 165109 (2010).
21. Altshuler, B. L., Ioffe, L. B. & Millis, A. J. Critical behavior of the $T = 0$ $2k_F$ density-wave phase transition in a two-dimensional Fermi liquid. *Phys. Rev. B* **52**, 5563–5572 (1995).
22. Metlitski, M. A. & Sachdev, S. Quantum phase transitions of metals in two spatial dimensions. II. Spin density wave order. *Phys. Rev. B* **82**, 075128 (2010).
23. Bergeron, D., Chowdhury, D., Punk, M., Sachdev, S. & Tremblay, A.-M. S. Breakdown of Fermi liquid behavior at the $(\pi, \pi) = 2k_F$ spin-density wave quantum-critical point: The case of electron-doped cuprates. *Phys. Rev. B* **86**, 155123 (2012).
24. Borisenko, S. V. *et al.* Two energy gaps and Fermi-surface “arcs” in NbSe_2 . *Phys. Rev. Lett.* **102**, 166402 (2009).
25. Jaramillo, R., Feng, Y., Wang, J. & Rosenbaum, T. F. Signatures of quantum criticality in pure Cr at high pressure. *Proc. Natl Acad. Sci. USA* **107**, 13631–13635 (2010).
26. Feng, Y., Jaramillo, R., Wang, J., Ren, Y. & Rosenbaum, T. F. High-pressure techniques for condensed matter physics at low temperature. *Rev. Sci. Instrum.* **81**, 041301 (2010).
27. Umeyayashi, H., Shirane, G., Frazer, B. C. & Daniels, W. B. Neutron diffraction study of Cr under high pressure. *J. Phys. Soc. Jpn* **24**, 368–372 (1968).
28. McWhan, D. B., Fleming, R. M., Moncton, D. E. & DiSalvo, F. J. Reentrant lock-in transition of the charge-density wave in $2H\text{-TaSe}_2$ at high pressure. *Phys. Rev. Lett.* **45**, 269–272 (1980).
29. Feng, Y. *et al.* Incommensurate antiferromagnetism in a pure spin system via cooperative organization of local and itinerant moments. *Proc. Natl Acad. Sci. USA* **110**, 3287–3292 (2013).
30. Ru, N. *et al.* Effect of chemical pressure on the charge density wave transition in rare-earth tritellurides RTe_3 . *Phys. Rev. B* **77**, 035114 (2008).
31. Berthier, C., Molinié, P. & Jérôme, D. Evidence for a connection between charge density waves and the pressure enhancement of superconductivity in $2H\text{-NbSe}_2$. *Solid State Commun.* **18**, 1393–1395 (1976).
32. Monceau, P., Ong, N. P., Portis, A. M., Meerschaut, A. & Rouxel, J. Electric field breakdown of charge-density-wave-induced anomalies in NbSe_3 . *Phys. Rev. Lett.* **37**, 602–606 (1976).
33. Lee, H. N. S., McKinzie, H., Tannhauser, D. S. & Wold, A. The low-temperature transport properties of NbSe_2 . *J. Appl. Phys.* **40**, 602–604 (1969).
34. McMillan, W. L. Microscopic model of charge-density-wave in $2H\text{-TaSe}_2$. *Phys. Rev. B* **15**, 643–650 (1977).
35. Kagoshima, S., Ishiguro, T. & Anzai, H. X-ray scattering study of phonon anomalies and superstructures in TTF-TNQ. *J. Phys. Soc. Jpn* **41**, 2061–2071 (1976).
36. Moncton, D. E., Axe, J. D. & DiSalvo, F. J. Neutron scattering study of the charge-density wave transition in $2H\text{-TaSe}_2$ and $2H\text{-NbSe}_2$. *Phys. Rev. B* **16**, 801–819 (1977).
37. Hill, J. P., Helgesen, G. & Gibbs, D. X-ray-scattering study of charge- and spin-density-waves in chromium. *Phys. Rev. B* **51**, 10336–10344 (1995).
38. Fukuyama, H. & Lee, P. A. Dynamics of the charge-density wave. I. Impurity pinning in a single chain. *Phys. Rev. B* **17**, 535–541 (1978).
39. Jensen, J. & Mackintosh, A. R. Helifan: A new type of magnetic structure. *Phys. Rev. Lett.* **64**, 2699–2702 (1990).
40. McMillan, W. L. Theory of discommensurations and the commensurate–incommensurate charge-density-wave phase transition. *Phys. Rev. B* **14**, 1496–1502 (1976).
41. Soumyanarayanan, A. *et al.* Quantum phase transition from triangular to stripe charge order in NbSe_2 . *Proc. Natl Acad. Sci. USA* **110**, 1623–1627 (2013).
42. Vanhoof, V., Rots, M. & Cottenier, S. Spin-density wave in Cr: Nesting versus low-lying thermal excitations. *Phys. Rev. B* **80**, 184420 (2009).
43. DiCarlo, D., Thorne, R. E., Sweetland, E., Sutton, M. & Brock, J. D. Charge-density-wave structure in NbSe_3 . *Phys. Rev. B* **50**, 8288–8296 (1994).
44. Schutte, W. J. & DeBoer, J. L. Valence fluctuations in the incommensurately modulated structure of calaverite AuTe_2 . *Acta Crystallogr. B* **44**, 486–494 (1988).
45. Sentef, M. *et al.* Examining electron-boson coupling using time-resolved spectroscopy. *Phys. Rev. X* **3**, 041033 (2013).
46. Schmitt, F. *et al.* Transient electronic structure and melting of a charge density wave in TbTe_3 . *Science* **321**, 1649–1652 (2008).
47. Makogon, D., Spielman, I. B. & Smith, C. M. Spin-charge-density wave in a rounded-square Fermi surface for ultracold atoms. *Europhys. Phys. Lett.* **97**, 33002 (2012).
48. Parker, C. V., Ha, L.-C. & Chin, C. Direct observation of effective ferromagnetic domains of cold atoms in a shaken optical lattice. *Nature Phys.* **9**, 769–774 (2013).
49. Feng, Y. *et al.* Energy dispersive X-ray diffraction of charge density waves via chemical filtering. *Rev. Sci. Instrum.* **76**, 063913 (2005).
50. Fleming, R. M., Moncton, D. E. & McWhan, D. B. X-ray scattering and electric field studies of the sliding mode conductor NbSe_3 . *Phys. Rev. B* **18**, 5560–5563 (1978).
51. Moudden, A. H., Axe, J. D., Monceau, P. & Levy, F. q_1 charge-density wave in NbSe_3 . *Phys. Rev. Lett.* **65**, 223–226 (1990).
52. Fleming, R. M., Schneemeyer, L. F. & Moncton, D. E. Commensurate–incommensurate transition in the charge-density-wave state of $\text{K}_{0.30}\text{MoO}_3$. *Phys. Rev. B* **31**, 899–903 (1985).

Acknowledgements

We are grateful for stimulating discussions with R. Jaramillo, C. V. Parker and M. R. Norman, and for NbSe_2 samples provided by Y. Liu and Z.-A. Xu. The work at the University of Chicago was supported by National Science Foundation Grant No. 1206519. The work at the Advanced Photon Source of Argonne National Laboratory was supported by the US Department of Energy Basic Energy Sciences under Contract No. NEAC02-06CH11357. J.v.W. acknowledges support from a VIDI grant financed by the Netherlands Organization for Scientific Research (NWO).

Author contributions

Y.F. and T.F.R. conceived the research. Y.F. and J.W. performed X-ray measurements. Y.F., D.M.S. and T.F.R. analysed the data. Y.F., J.v.W., F.F. and P.B.L. developed the theoretical framework. Y.F., J.v.W. and T.F.R. prepared the manuscript. All authors commented on the manuscript.

Additional information

Supplementary information is available in the [online version of the paper](#). Reprints and permissions information is available online at www.nature.com/reprints.

Correspondence and requests for materials should be addressed to Y.F. or T.F.R.

Competing financial interests

The authors declare no competing financial interests.

Methods

X-ray diffraction. Both ambient and high-pressure X-ray diffractions were performed at beamline 4-ID-D of the Advanced Photon Source. 18.85 keV X-rays were used, chosen to lie below the Nb K-edge to avoid this fluorescence excitation. The X-ray beam was focused to a full-width at half-maximum size of 250×120 (H \times V) μm^2 using Pd-coated mirrors and further narrowed by motorized slits for high-pressure work. For high-resolution longitudinal scans, a vertical detector slit size of 0.1 or 0.2 mm was used, with a sample-to-slit distance of 1.25 m. Diffraction in the vertical plane thus had a maximal momentum-space resolution of about $1 \times 10^{-3} \text{ \AA}^{-1}$. Both ambient and high-pressure diffraction were performed in the transmission geometry to the a - b plane of NbSe₂ for bulk sensitivity. At ambient pressure, a Vortex Si-drift detector was used to reject Se K-fluorescence. For the high-pressure study, a Cyberstar NaI X-ray detector was used for a higher counting efficiency, as the diamond anvils absorb the majority of

the Se K-fluorescence. Both X-ray detectors have only coarse energy resolutions of 0.1–1 keV. However, the spanned solid angle of $1\text{--}3 \times 10^{-7} \text{ sr}$ by our detector slits effectively eliminated the detected intensity of inelastic scattering of dynamic CDW fluctuations. Thus, our observed CDW diffraction near the quantum critical point represents the static order, in comparison to the quasi-elastic nature of resonant X-ray scattering techniques³.

Sample and high-pressure environment. Single crystals of NbSe₂ were used in as-grown condition at ambient pressure. The thickness of ambient pressure samples, varying from 40 to 75 μm , matches well with one X-ray absorption length of our X-rays. For high-pressure measurements, single crystals were prepared by blade dicing to a typical size of $80 \times 80 \times 50 \mu\text{m}^3$. A methanol:ethanol 4:1 mixture was used as the pressure medium. More details can be found in refs 5,26.

Itinerant density wave instabilities at classical and quantum critical points

Yejun Feng^{1,2}, Jasper van Wezel³, Jiyang Wang², Felix Flicker⁴, D. M. Silevitch²,
P. B. Littlewood^{2,5}, T. F. Rosenbaum^{2,6}

¹The Advanced Photon Source, Argonne National Laboratory, Argonne, Illinois 60439, USA

²The James Franck Institute and Department of Physics, The University of Chicago, Chicago, Illinois 60637, USA

³Institute for Theoretical Physics, University of Amsterdam, 1090 GL Amsterdam, The Netherlands

⁴H. H. Wills Physics Laboratory, University of Bristol, Bristol BS8 1TL, UK

⁵Physical Sciences and Engineering, Argonne National Laboratory, Argonne, Illinois 60439, USA

⁶Division of Physics, Mathematics, and Astronomy, California Institute of Technology, Pasadena, California 91125, USA

NUMERICAL EMULATION OF $Q(T, P)$ EVOLUTION IN NbSe₂

a. Construction of CDW phase distortion using McMillan's discommensuration model

A distortion $\Delta\phi(x)$ of the CDW phase $\phi(x)$ from a purely sinusoidal form, engages the lock-in term $f\psi^n \cos(n\phi - Gx)$ in Eq. 1 and results in the presence of higher harmonics of the primary wave. A growing phase distortion effectively interpolates between an incommensurate CDW at the Q -vector preferred by the full susceptibility and a commensurate CDW locked into the lattice [40]. Our diffraction results (Fig. 3b, 6c) provide the relative intensities but not the relative phases between harmonics, and hence it is not possible to experimentally reconstruct $\Delta\phi(x)$. To simulate $Q(T, P)$ as we show in Fig. 5, we use McMillan's discommensuration model [40] to construct a functional form of $\Delta\phi(x)$ for smooth and wide phase distortions. The CDW phase $\phi(x)$ is expressed using a limited number (i.e. two) of parameters:

$$\phi_{discomm}(x) = 2\pi\left(\frac{1}{3} + \alpha\left(q - \frac{1}{3}\right)\right)x - \frac{1}{3}\sum_n \frac{\beta^n}{n} \sin(2\pi n(1 - 3q)\alpha x). \quad (\text{S1})$$

Here, x and q are written in units of the real and reciprocal and space lattice constants, respectively. With $\beta = 0$, Eq. S1 represents a perfectly sinusoidal wave, with a varying wave vector determined by α . At $\alpha = 0$, the CDW is locked in at the commensurate wave vector of $1/3$ r.l.u., while for $\alpha = 1$, the CDW propagates at the natural, incommensurate q value preferred by the susceptibility, which equals the experimentally measured wave vector $Q(T_{\text{DW}}, P)$ (purple dashed line in Fig. 1a). For nonzero values of β , the perfect sinusoidal CDW is distorted, and $2\pi/3$ phase slips appear at spatial separations of

$\xi_0 = \frac{1}{3\delta} = \frac{1}{[(1-3q)\alpha]}$. The parameter β controls the width of these distortions. For $\beta = 1$, the phase slips are infinitely narrow, and the function $\phi(x)$ is a series of straight lines with slope $\frac{2\pi}{3}$ separated by sharp steps. For $\beta < 1$, the steps become smooth, and the phase distortions obtain a finite width.

b. Determining parameters by minimization of free energy and global $Q(T, P)$ behavior

The free energy F (Eq. 1) can be minimized with respect to the parameters α and β for any given set of coefficients a, b, e, f , and q . During the minimization, we approximate the amplitude of the CDW to be fixed by the first two terms in F , so that $\psi^2 = \frac{a}{2b}$, which is justified as long as $e, f \ll b$. The values of α and β that minimize the spatially integrated free energy F thus are only a function of $\frac{f}{e}\psi$ and q . In these numerical minimizations, we retained 200 powers of β in the functional form of Eq. (S1), and employed a real space grid of 250,000 sites, covering 5,000 atoms.

In the free energy minimization process described above, we notice α and β are smoothly varying as a function of $\frac{f}{e}\psi$ and q . To reduce computation time, the free energy minimization was performed at selected values of $\frac{f}{e}\psi$ and q , and smooth interpolating functions were used to generate α and β values in successive calculations.

The constraints imposed on the parameters a, b, e, f , and q in the free energy F (Eq. 1) over the pressure-temperature space are discussed in the main text, based on physical considerations. As mentioned, there are consequently only two parameters left to determine $Q(T, P)$. They are related to the competition between the fourth and fifth terms in Eq. 1, with the coefficient f approximated as $f(P) = f_0 + f_1P$. The first parameter is the ratio $\frac{f_0}{e}$, which sets the evolution of the phase distortions at ambient pressure, and hence $Q(T, P=0)$. The coefficient f_1 dictates the evolution under pressure. We chose the first parameter so the range of simulated $Q(T, P=0)$ equals that of the experimental results. Subsequently, we chose the value of f_1 such that $Q(T=0, P)$ reaches the turning point of its non-monotonic evolution at about 2.3 GPa, similar to the experimental results at 3.5 K (Fig. 1a). The resulting simulated $Q(T, P)$ is shown in Fig. 5.

c. Characteristics of simulated CDW states

Having optimized the temperature and pressure dependence of $Q(T, P)$ we now discuss a few characteristics of the simulated CDW states, which follow from the corresponding temperature and pressure dependencies of the parameters α and β .

The simulated $Q(T, P=0)$ is presented in Fig. S1. Although the shape and curvature are different from that seen in the experimental data (Fig. 2a), the overall monotonically changing trend is preserved. The difference between simulation and

experiment is due to the combination of restricting the functional form of $\phi(x)$ in Eq. S1, and the linear temperature dependence of the coefficient a .

The real space charge modulation $\psi \cos(\phi(x))$ can be Fourier transformed (FT) to directly simulate the experimentally observed diffraction pattern, as the intensity I is proportional to the square of the FT amplitude. Two representative spectra at ambient pressure are presented in Fig. S2. To increase the precision with which we can determine the peak heights, we oversampled the FT. This allows us to get a dense set of data points around the incommensurate peak positions, but it also results in ringing near the tails of all peaks, as a consequence of the Nyquist effect. Nevertheless, higher harmonics in Fourier space are observed as expected from the simulated phase distortion of Eq. S1. In Fig. S3, we plot intensity ratios of four strongest harmonics to the primary wave as a function of temperature at ambient pressure. We notice the intensity ratio of second harmonic to the primary peak reaches 0.037 at base temperature, in comparison to 0.012 of experimental results (Fig. 4 inset). Although the intensity of harmonics tends to drop with increasing distance from the main peak (see Fig. S3), the intensities of the fourth, fifth, seventh, and tenth harmonics lie above the experimental sensitivity limit of $\sim 10^{-4}$ (see Fig. 3 and Fig. 6c). The presence of these additional harmonics can be attributed to the restricted functional form imposed for $\phi(x)$ by Eq. S1. Nevertheless, the trend of the harmonic ratios as a function of temperature is qualitatively correct. The intensity ratios are the largest at base temperature, and monotonically disappear as the transition temperature is approached.

For CDW states under pressure, our experimentally measured primary CDW has a signal to noise ratio much less than 50:1 (Ref. [5], Fig. 6b), mostly due to an increased elastic scattering background from diamond anvils as a part of the high pressure sample environment. Thus it is insufficient to reveal higher harmonics. Nevertheless, simulation can provide qualitatively predictions of the higher harmonics behavior. As the simulated CDW becomes commensurate for a finite pressure range at base temperature (Fig. 5), the harmonic ratios cannot be unambiguously defined. Instead, we plot the harmonic ratios at $T = 9.4$ K, a temperature which is about $1/3$ of T_c at ambient pressure (Fig. S4). We notice that the harmonic ratio is also non-monotonic. The simulation and experiment agree that the CDW is always a perfect sine wave without any phase distortions or higher harmonics at $T = T_{\text{CDW}}(P)$.

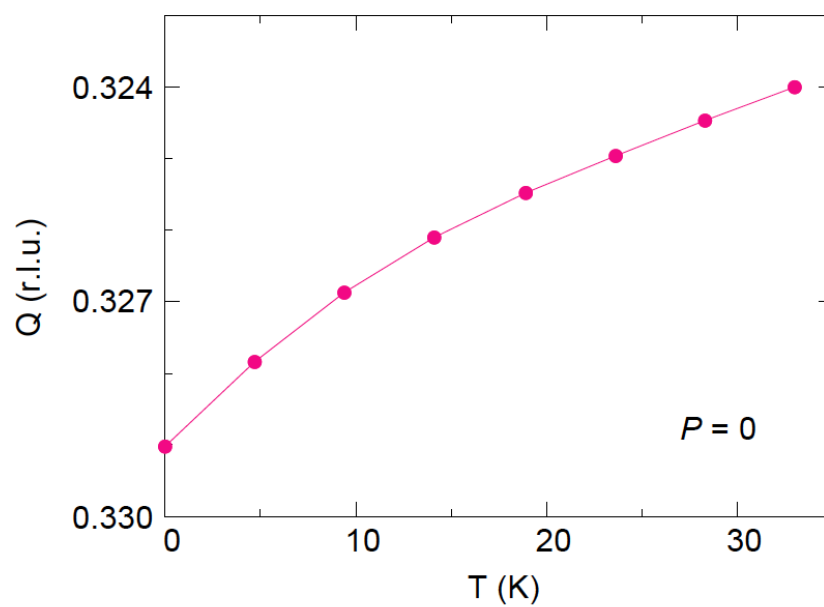


Fig. S1: Simulated $Q(T)$ evolution of NbSe₂ at ambient pressure.

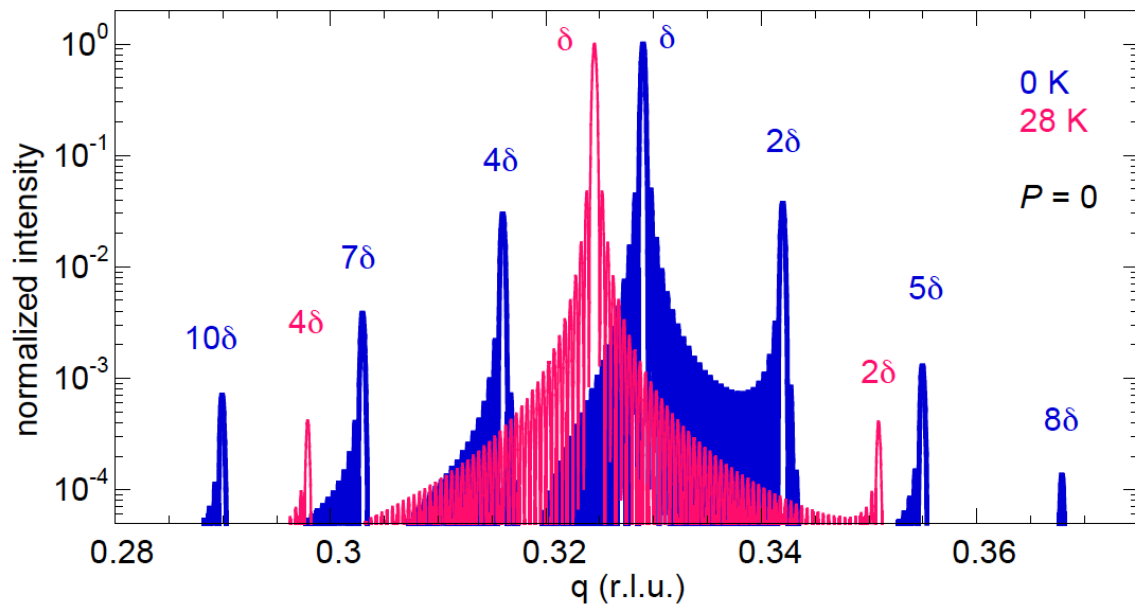


Fig. S2: Simulated CDW diffraction profiles Fourier transformed from simulated CDW states at 0 K and 28 K. They represent β values of 0.54 and 0.054 respectively.

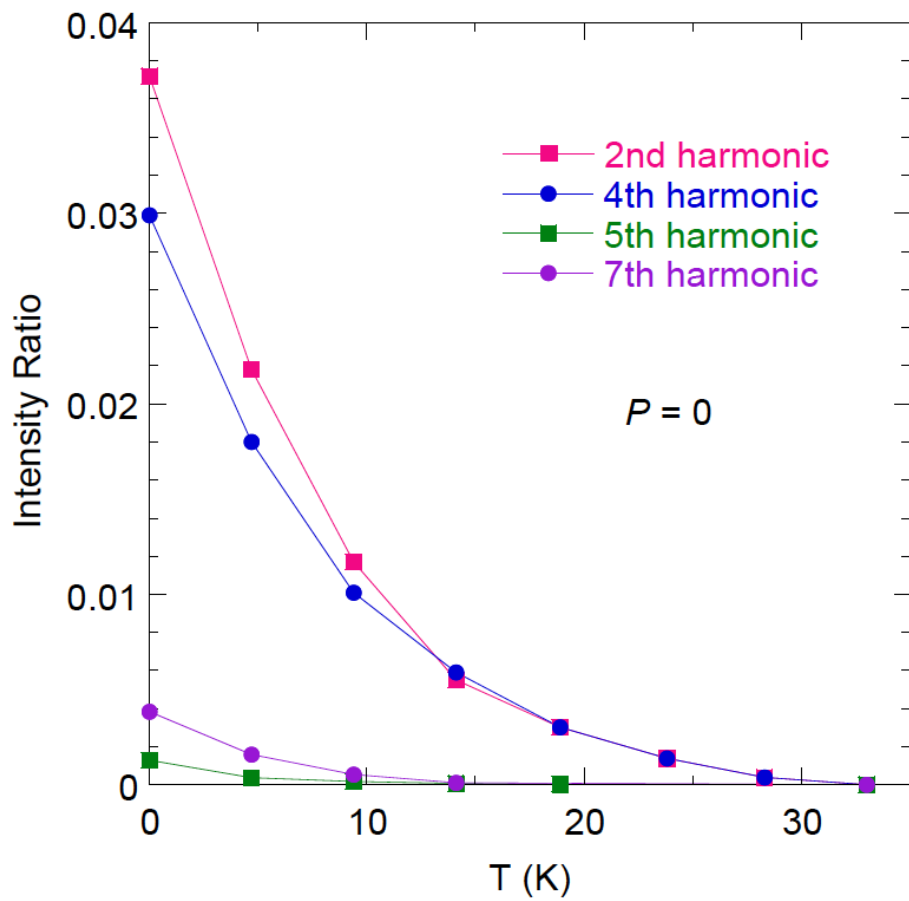


Fig. S3: Temperature evolutions of intensity ratio of higher harmonics to the primary CDW.

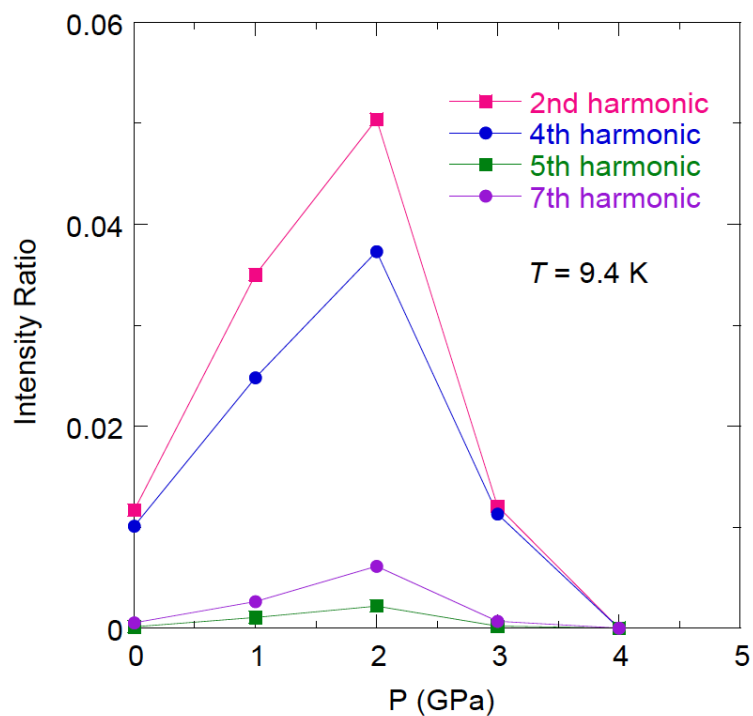


Fig. S4: Pressure evolutions of intensity ratio of higher harmonics to the primary CDW, taken at 9.4K.